The Astrophysical Journal Letters, 940:L5 (11pp), 2022 November 20 https://doi.org/10.3847/2041-8213/ac961c

GOALS-JWST: Resolving the Circumnuclear Gas Dynamics in NGC 7469 in the Mid-infrared

Vivian U[1], Thomas Lai[2], Marina Bianchin[1,3], Raymond P. Remigio[1], Lee Armus[2], Kirsten L. Larson[4], Tanio Díaz-Santos[5,6], Aaron Evans[7,8], Sabrina Stierwalt[9], David R. Law[10], Matthew A. Malkan[11], Sean Linden[12], Yiqing Song[7,8,13], Paul P. van der Werf[14], Tianmu Gao[15], George C. Privon[7,16], Anne M. Medling[17,18], Loreto Barcos-Muñoz[7,8], Christopher C. Hayward[19], Hanae Inami[20], Jeff Rich[21], Susanne Aalto[22], Philip Appleton[2], Thomas Bohn[20], Torsten Böker[23], Michael J. I. Brown[24], Vassilis Charmandaris[5,6,25], Luke Finnerty[11], Justin Howell[2], Kazushi Iwasawa[26,27], Francisca Kemper[27,28,29], Jason Marshall[30], Joseph M. Mazzarella[2], Jed McKinney[31,32], Francisco Muller-Sanchez[33], Eric J. Murphy[7], David Sanders[34], and Jason Surace[2]

[1] Department of Physics and Astronomy, 4129 Frederick Reines Hall, University of California, Irvine, CA 92697, USA; vivianu@uci.edu
[2] IPAC, California Institute of Technology, 1200 E. California Boulevard, Pasadena, CA 91125, USA
[3] Universidade Federal de Santa Maria, Departamento de Física, Centro de Ciências Naturais e Exatas, 97105-900, Santa Maria, RS, Brazil
[4] AURA for the European Space Agency (ESA), Space Telescope Science Institute, 3700 San Martin Drive, Baltimore, MD 21218, USA
[5] Institute of Astrophysics, Foundation for Research and Technology-Hellas (FORTH), Heraklion, 70013, Greece
[6] School of Sciences, European University Cyprus, Diogenes street, Engomi, 1516 Nicosia, Cyprus
[7] National Radio Astronomy Observatory, 520 Edgemont Road, Charlottesville, VA 22903, USA
[8] Department of Astronomy, University of Virginia, 530 McCormick Road, Charlottesville, VA 22903, USA
[9] Physics Department, 1600 Campus Road, Occidental College, Los Angeles, CA 90041, USA
[10] Space Telescope Science Institute, 3700 San Martin Drive, Baltimore, MD 21218, USA
[11] Department of Physics & Astronomy, 430 Portola Plaza, University of California, Los Angeles, CA 90095, USA
[12] Department of Astronomy, University of Massachusetts at Amherst, Amherst, MA 01003, USA
[13] European Southern Observatory, Alonso de Cordova 3107, Santiago, Chile
[14] Leiden Observatory, Leiden University, PO Box 9513, 2300 RA Leiden, The Netherlands
[15] Department of Astronomy, Beijing Normal University, Beijing 100875, People's Republic of China
[16] Department of Astronomy, University of Florida, P.O. Box 112055, Gainesville, FL 32611, USA
[17] Department of Physics & Astronomy and Ritter Astrophysical Research Center, University of Toledo, Toledo, OH 43606, USA
[18] ARC Centre of Excellence for All Sky Astrophysics in 3 Dimensions (ASTRO 3D); Australia
[19] Center for Computational Astrophysics, Flatiron Institute, 162 Fifth Avenue, New York, NY 10010, USA
[20] Hiroshima Astrophysical Science Center, Hiroshima University, 1-3-1 Kagamiyama, Higashi-Hiroshima, Hiroshima 739-8526, Japan
[21] The Observatories of the Carnegie Institution for Science, 813 Santa Barbara Street, Pasadena, CA 91101, USA
[22] Department of Space, Earth and Environment, Chalmers University of Technology, SE-412 96 Gothenburg, Sweden
[23] European Space Agency, Space Telescope Science Institute, 3700 San Martin Drive, Baltimore, MD 21218, USA
[24] School of Physics and Astronomy, Monash University, Clayton, VIC 3800, Australia
[25] Department of Physics, University of Crete, Heraklion, 71003, Greece
[26] Institut de Ciències del Cosmos (ICCUB), Universitat de Barcelona (IEEC-UB), Martí i Franquès, 1, E-08028 Barcelona, Spain
[27] ICREA, Pg. Lluís Companys 23, E-08010 Barcelona, Spain
[28] Institut de Ciencies de l'Espai (ICE, CSIC), Can Magrans, s/n, E-08193 Bellaterra, Barcelona, Spain
[29] Institut d'Estudis Espacials de Catalunya (IEEC), E-08034 Barcelona, Spain
[30] Glendale Community College, 1500 N. Verdugo Road, Glendale, CA 91208, USA
[31] Department of Astronomy, University of Massachusetts, Amherst, MA 01003, USA
[32] Department of Astronomy, The University of Texas at Austin, 2515 Speedway Boulevard, Stop C1400, Austin, TX 78712, USA
[33] Department of Physics and Materials Science, The University of Memphis, 3720 Alumni Avenue, Memphis, TN 38152, USA
[34] Institute for Astronomy, University of Hawaii, 2680 Woodlawn Drive, Honolulu, HI 96822, USA
Received 2022 September 2; revised 2022 September 28; accepted 2022 September 29; published 2022 November 14

Abstract

The nearby, luminous infrared galaxy NGC 7469 hosts a Seyfert nucleus with a circumnuclear star-forming ring and is thus the ideal local laboratory for investigating the starburst–AGN (active galactic nucleus) connection in detail. We present integral-field observations of the central 1.3 kpc region in NGC 7469 obtained with the JWST Mid-InfraRed Instrument. Molecular and ionized gas distributions and kinematics at a resolution of ∼100 pc over the 4.9–7.6 μm region are examined to study the gas dynamics influenced by the central AGN. The low-ionization [Fe II] λ5.34 μm and [Ar II] λ6.99 μm lines are bright on the nucleus and in the starburst ring, as opposed to H_2 S(5) λ6.91 μm, which is strongly peaked at the center and surrounding ISM. The high-ionization [Mg V] line is resolved and shows a broad, blueshifted component associated with the outflow. It has a nearly face-on geometry that is strongly peaked on the nucleus, where it reaches a maximum velocity of -650 km s^{-1}, and extends about 400 pc to the east. Regions of enhanced velocity dispersion in H_2 and [Fe II] ∼ 180 pc from the AGN that also show high $L(H_2)/L(\mathrm{PAH})$ and $L([\mathrm{Fe\ II}])/L(\mathrm{Pf}\alpha)$ ratios to the W and N of the nucleus pinpoint regions where the ionized outflow is depositing energy, via shocks, into the dense interstellar medium between the nucleus and the starburst ring. These resolved mid-infrared observations of the nuclear gas dynamics demonstrate the power of JWST and its

high-sensitivity integral-field spectroscopic capability to resolve feedback processes around supermassive black holes in the dusty cores of nearby luminous infrared galaxies.

1. Introduction

Accreting supermassive black holes (SMBHs) within active galactic nuclei (AGNs) are thought to play a prominent role in influencing the interstellar medium (ISM) of their host through feedback mechanisms such as outflows (see reviews by Veilleux et al. 2020; Armus et al. 2020). Distinguishing the drivers of such winds and determining their direct impacts on the surrounding star formation has been difficult due to observational challenges such as heavy dust obscuration. Investigating the triggering of AGN outflows is most ideally done close to the launching site, which is often obscured by dust in the case of many Seyfert and luminous infrared galaxies (LIRGs; $L_{\rm IR} \geqslant 10^{11} L_{\odot}$), with the latter exhibiting extinction upward of $A_V \sim 40$ mag or higher (Mattila et al. 2007; Väisänen et al. 2017; U et al. 2019; Falstad et al. 2021; Pérez-Torres et al. 2021).

NGC 7469 offers a prime opportunity to study these phenomena in detail. It is a nearby ($z = 0.01627$; $D_L = 70.6$ Mpc)[35] LIRG hosting a bright Seyfert 1.5 nucleus (Landt et al. 2008) surrounded by a starburst ring ($R_{\rm peak} \sim$ 530 pc; Genzel et al. 1995; Song et al. 2021) with a bimodal age distribution of stellar populations (Díaz-Santos et al. 2007). Evidence of a wide-angle E–W biconically illuminated outflow in the near-infrared coronal line [Si VI] $\lambda 1.96\,\mu$m ($R_{\rm [Si\ VI]} = 90$ pc) has been presented using VLT/SINFONI integral-field spectroscopy (IFS) (FWHM $= 0\farcs14$, or 46 pc; Müller-Sánchez et al. 2011). The characteristic outflow structure with broad and blueshifted components along the minor axis of the galactic disk was not seen in the coarser optical GTC/MEGARA IFS observations (FWHM $= 0\farcs93$, or 307 pc; Cazzoli et al. 2020). However, turbulent, noncircular kinematics, detected in a component of the Hα–[N II] complex within the central 610 pc, might be associated with it. More recently, extended circumnuclear outflows were found reaching 531 pc from the AGN in VLT/MUSE observations of [O III] λ5007 Å (FWHM $= 1\farcs23$, or 406 pc; Robleto-Orús et al. 2021; Xu & Wang 2022). ALMA observations of CO(1−0), CO(2−1), and [C I] in the inner ∼2 kpc region with angular resolutions of $0\farcs35$ (120 pc) show largely rotational kinematics (Izumi et al. 2020; Nguyen et al. 2021). Despite the multiwavelength effort, there is still no clear picture for how the putative outflow interacts with the circumnuclear gas and starburst ring.

With JWST's 6.5 m mirror and advanced instrument suite, we can now resolve the dynamics of gas and dust at angular resolution of $\sim 0\farcs2 - 0\farcs8$ in the mid-infrared wavelengths (5−28 μm). In particular, this Letter investigates the detailed gas kinematics in the inner 600 pc region (the "inner ISM region" hereafter) of NGC 7469. We first describe the observations and data processing in Section 2. Section 3 highlights the moment maps of several key ionized and molecular gas emission lines and demonstrates the richness of features in the mid-infrared spectra extracted from the inner ISM region. In Section 4, we discuss the properties of the detected outflow and the shock excitation in the ISM. In several companion papers, we investigate the infrared spectral properties of the AGN (Armus et al. 2022), the starburst ring (Lai et al. 2022), and the circumnuclear star-forming regions (Bohn et al. 2022) in NGC 7469.

Throughout the paper, $H_0 = 70$ km s^{-1} Mpc^{-1}, $\Omega_{\rm m} = 0.30$, and $\Omega_{\rm vac} = 0.70$ have been adopted. At the redshift of $z = 0.01627$, $1'' = 330$ pc (Wright 2006).

2. Observations and Data Reduction

Mid-infrared IFS observations of NGC 7469 were taken with the JWST Mid-InfraRed Instrument (MIRI; Rieke et al. 2015; Labiano et al. 2021) in Medium Resolution Spectroscopy (MRS) mode on 2022 July 3–4 UT as part of the Early Release Science (ERS) Program 1328 (Co-PIs: L. Armus and A. Evans). The observations covered the full 4.9−28.8 μm range using the short (A), medium (B), and long (C) subbands in all four channels. We adopted the FASTR1 readout pattern to optimize the dynamic range expected in the observations. Using the extended source 4 pt dither pattern, the science exposure time per subband was 444 s. Because our source is extended, we linked the observation to a dedicated background with the same observational parameters in all three grating settings.

Uncalibrated science and background observations were downloaded using the MAST Portal and processed with the JWST Science Calibration Pipeline (Bushouse et al. 2022) version 1.6+ in batch mode. The `Detector1` pipeline applies detector-level corrections and ramp fitting to the individual exposures. The output rate images were subsequently processed outside the JWST pipeline to flag newly-acquired bad pixels and additional cosmic-ray artifacts and to remove vertical stripes and zero-point residuals remaining after the pipeline dark subtraction. These additional corrections broadly follow the steps taken for JWST ERO observations as described by Pontoppidan et al. (2022). The resulting rate files are then processed with the JWST `Spec2` pipeline for distortion and wavelength calibration, flux calibration, and other 2D detector-level steps. Residual fringe corrections using prototype pipeline code have been applied to both the Stage 2 products and to the 1D spectra resulting from Stage 3 processing.

Stage 3 processing (`Spec3`) performs background subtraction before combining data from multiple exposures into the final data cubes. Background light is subtracted from the 2D science images using a master background frame generated from our associated background observations. The master background is a 1D median sigma-clipped spectrum calculated over the field of view (FOV) of the background observations and projected to the entire 2D detector array. Since it is a combination of many detector pixels, it does not degrade the signal-to-noise ratio (S/N) the way a pixel-by-pixel background subtraction would. The cube-building step in `Spec3` assembles a single 3D data cube from all of the individual 2D calibrated detector images, combining data across individual wavelength bands and channels.

NIRCam's broadband F150W, F200W, and F444W images of NGC 7469 from our ERS-1328 program have been included in this paper for visualization purposes. Readers are referred to Bohn et al. (2022) for the data-processing details.

[35] NED.

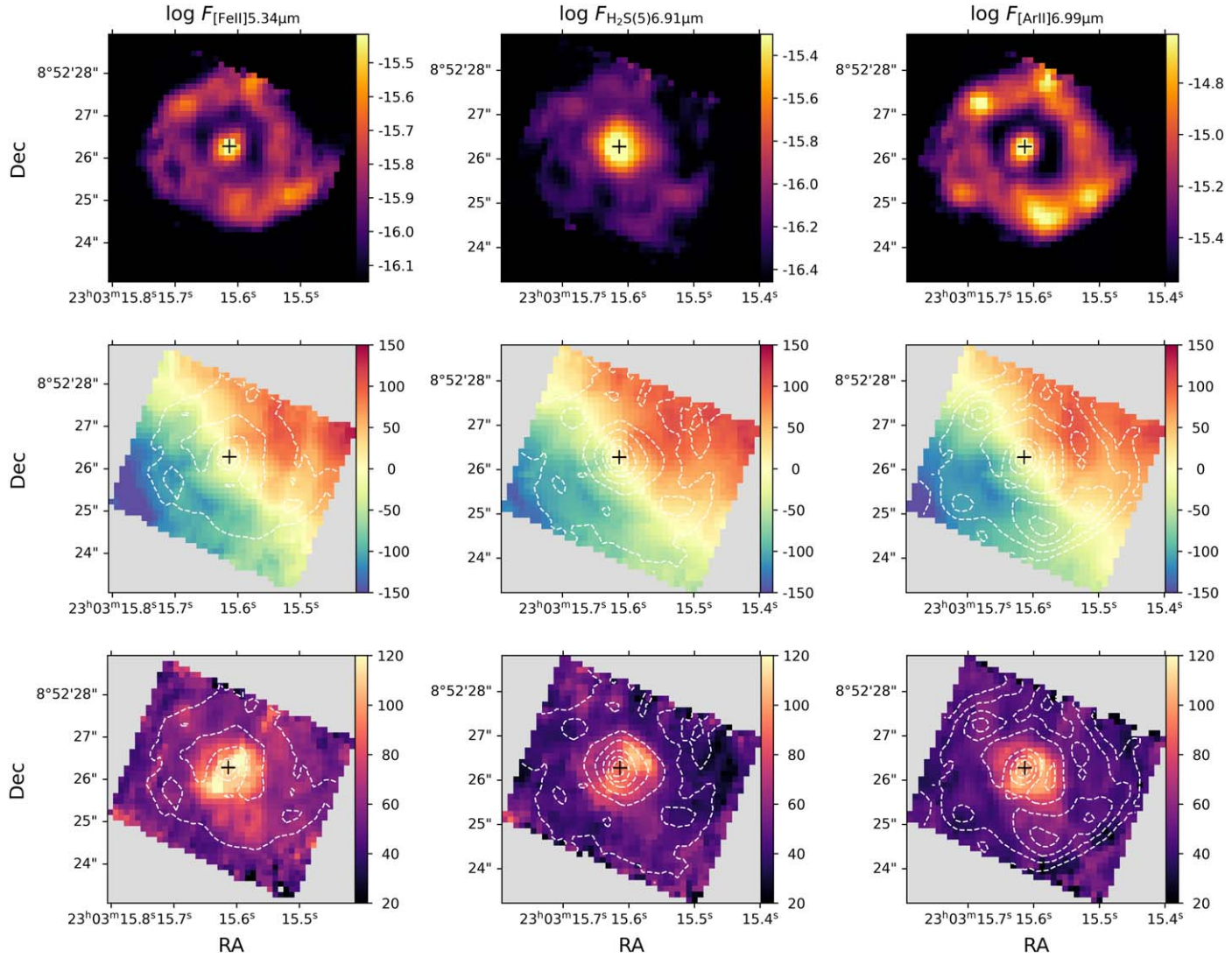

Figure 1. The distribution of flux (top; in log erg s^{-1} cm^{-2} $pixel^{-1}$), velocity (middle; in km s^{-1}), and velocity dispersion (bottom; in km s^{-1}) for several bright emission lines in Ch1: [Fe II] λ5.34 μm (left), H_2 S(5) λ6.91 μm (middle), [Ar II] λ6.99 μm (right). Contours based on the flux distribution are overlaid on the kinematic maps of the respective gas species. The black cross marks the peak of the H_2 emission. North is up and east is to the left. The distributions of the molecular and ionized gas emission are strikingly different, with H_2 being preferentially bright at the center while [Fe II] and [Ar II] appear clumpy at the star-forming ring. H_2 and [Fe II] exhibit enhanced dispersion $\sim$180 pc off the nucleus.

3. Analysis and Results

3.1. Emission-line Maps

In this paper, we focus our investigation on the Channel 1 MRS data (4.89 μm to 7.66 μm), which hosts key diagnostic lines for shock excitation ([Fe II] and H_2), strength of the radiation field ([Ar II]), and coronal region ([Mg V]) at the highest spatial resolution afforded by MRS at 0.″3. Known issues with MRS wavelength solutions (at the time of this writing) are generally not a concern for Ch 1, where zero-point variations at the 0.001 μm level ($\sim$60 km s^{-1}) are within the spectral noise at these wavelengths. We fit single Gaussian profiles to three of the brightest ionized and molecular lines in Ch 1 ([Fe II] λ5.34 μm, H_2 S(5) λ6.91 μm, and [Ar II] λ6.99 μm) on a spaxel-by-spaxel basis and computed their corresponding flux, velocity, and velocity dispersion maps using `ifscube` (Ruschel-Dutra & Dall'Agnol De Oliveira 2020; Ruschel-Dutra et al. 2021). We correct our line-width measurements for instrumental broadening ($\sigma_{inst} = 36.5$ km s^{-1}) by subtracting it in quadrature.

As shown in Figure 1, the morphologies of the emission lines differ among these molecular and low-ionization potential (IP) gases: [Fe II] (IP = 7.9 eV) and [Ar II] (IP = 15.8 eV) are bright and compact at the nucleus and at several star-forming clumps in the ring. The starburst ring appears slightly asymmetric around the central nucleus, where the southeast (SE) inner edge is closer to the AGN. In contrast, H_2 dominates and appears extended at the center but relatively weak in the ring. The nuclear H_2 emission is $\sim$1.″4 across, nearly five times larger than the FWHM of the point-spread function (PSF) of 0.″3 at 7.2 μm continuum. Filamentary structures extend in the NE and SW directions from the central emission that appear to be well aligned with high-surface-brightness CO gas (see Figure 2 in Izumi et al. 2020) at the sites of the innermost spiral arms.

The gas kinematics for these lines are largely similar, sharing a bulk rotational motion around the ring. The kinematic major axis has a position angle (PA) of 126° as measured using `PaFit` (Krajnovic et al. 2006). The morphological semimajor

axis (2.″1) and semiminor axis (1.″7) of the ring gives an inclination angle $i = 51°$. The velocity field is reminiscent of a tilted rotating ring with the near (far) side in the E/NE (W/SW). We compute the contribution to the velocity dispersion due to rotation and beam smearing following the technique from Swinbank et al. (2012) and De Breuck et al. (2014): We measure the luminosity-weighted velocity gradient across the FWHM of the beam at each spaxel and subtracted it from the velocity dispersion in quadrature. For all these gases, the median effect was at the 6% level (∼4 km s^{-1}), with 75% of the spaxels affected under 10% (∼7 km s^{-1}) and 95% under 20% (∼14 km s^{-1}). The H_2 velocity dispersion is slightly suppressed at the center (95 km s^{-1}, or 75 km s^{-1} intrinsically) but increases toward the NW direction in a cone shape, similar to the shocked H_2 λ2.12 μm detected in Mrk 273 (U et al. 2013). The [Fe II] gas, sensitive to strong shocks, shows high velocity dispersions (reaching as high as 135 km s^{-1}) roughly along the kinematic axis toward both NW and SE.

3.2. Spectral Fits

To quantify the ISM conditions surrounding the AGN, we divide the inner 1.″8 (600 pc) ISM region within the ring as seen at 7.1 μm, the observed wavelength of [Ar II], into a 3 × 3 grid and subsequently extract 1D spectra from these bins. Since the central region contains a point source from the AGN, we apply a wavelength-dependent aperture correction to the central spectrum. The aperture correction is calculated using the MRS PSF models from WebbPSF (Oschmann et al. 2014) that have been adjusted to match preliminary in-flight performance during JWST commissioning (private communication). These models are nearly diffraction limited longward of 8 μm and moderately elliptical at shorter wavelengths. Figure 2 shows the extraction regions (0.″6 on a side) and their corresponding spectra normalized at [Ar II]. The stitched Ch 1 short–medium–long spectra exhibit a number of strong molecular and fine-structure lines, as well as polycyclic aromatic hydrocarbon (PAH) features. Several of these emission lines were previously seen with Spitzer/IRS, but with a large aperture that included the starburst ring and the AGN (Inami et al. 2013; Stierwalt et al. 2013). The relatively poor spatial resolution of Spitzer precluded studies of the variations in the strengths and profile shapes of these lines with positions on these scales, now made possible with JWST. Detailed discussions of the nuclear AGN spectrum and of the dust grains in the star-forming ring are presented in two companion papers (Armus et al. 2022; Lai et al. 2022, respectively).

A handful of high-ionization lines ([Fe VIII] λ5.48 μm with IP = 124 eV, [Mg VII] λ5.50 μm with IP = 186 eV, and [Mg V] λ5.61 μm with IP = 109 eV) show clear blueshifted wings. The coronal line [Mg V] is the strongest among these features in all the 1D spectra. Given their high IPs, photoionized coronal lines are typically produced on several hundred parsecs away from the AGN (Ferguson et al. 1997). Kinematics of coronal lines often reveal blueshifts indicating that outflows on these scales are common (e.g., Riffel et al. 2021). While strong coronal lines might be expected at the nucleus, broad and blueshifted components may be present in the immediate vicinity of the nucleus if an outflow is present. Indeed, a close look at our extracted spectra reveals that [Mg V] is most significantly shifted in the E, 70 km s^{-1} with respect to the center (Figure 2 inset). The blueshifted asymmetric profile of [Mg V] can be seen in several other directions as well.

To further investigate the distribution and kinematics of [Mg V], we fit two Gaussian components using a modified version of the Bayesian AGN Decomposition Analysis for SDSS Spectra software package (BADASS; Sexton et al. 2021) spaxel by spaxel and generate moment maps for the two components; see the Appendix. The core, narrow component of [Mg V] is plausibly consistent with rotation at the same position angle as that for the low-ionization and molecular gases. A broad component is identified in a subset of the central spaxels, encompassing the blueshifted outflowing gas. The outflow is detected up to a projected distance of ∼420 pc E of the nucleus. Within this physical extent, the gas exhibits a median line-of-sight velocity of $v_{\rm med} = -205$ km s^{-1} but reaching as high as −650 km s^{-1} close to the AGN. This outflow is also identified in other high-ionization lines such as [Fe VIII] λ5.45 μm (IP = 124 eV) and [Ne VI] λ7.65 μm (IP = 126 eV), and mid-ionization lines such as [O IV] λ25.9 μm (IP = 55 eV), the detailed line profiles for which will be characterized in Armus et al. (2022). We do find that the high-ionization lines in the nuclear spectrum exhibit extreme blueshifted velocities upward of 1000 km s^{-1}, indicating the presence of very fast winds at the center.

Multicomponent spectral fitting is performed on the full Ch 1 spectral coverage of each 1D spectrum using the Continuum And Feature Extraction (CAFE; Marshall et al. 2007; T. Díaz-Santos et al. 2022, in preparation) software package originally written in IDL for analyzing Spitzer/IRS data. While individual atomic or molecular lines can be fit using single or double Gaussian profiles, CAFE specializes in decomposing the emission in the mid-infrared regime into AGNs, PAHs, dust of different temperatures, and starburst components and is ideal for recovering properties of PAH features in 1D spectra that often require multiple components to fit correctly. The development of an improved version of the CAFE code that handles high-resolution spectral decomposition is fully described in T. Díaz Santos et al. (2022, in preparation). Major updates include a fully functional Python version applicable to the data format and spectral resolution of JWST IFS data. The flux densities for the various relevant emission-line features are reported in Table 1.

4. Discussion

4.1. Outflow Characteristics

As briefly introduced in Section 1, previous multiwavelength efforts in the literature converged on the presence of nonrotational kinematics in the circumnuclear region of NGC 7469, but the picture of how the nonrotating gas behaved at different physical scales was incomplete due to mismatches in observational parameters and data sensitivity (Müller-Sánchez et al. 2011; Cazzoli et al. 2020; Robleto-Orús et al. 2021). With JWST's superb sensitivity, spectral resolution, and integral-field capability in the mid-infrared wavelengths, we can now incorporate the molecular, low-, and high-ionization gases into a coherent picture with the same data set on the same physical scales. We see from Figure 2 that the high-IP [Mg V] line is prominently blueshifted, with a nearly face-on geometry and flux extending E of the nucleus. The intensity of the broad, blueshifted component from Figure A2 (lower left panel) is overplotted on the NIRCAM images as contours in Figure 3 (inset).

Given that the gas is photoionized and [Mg V] is tracing the illumination pattern, we see primarily the blueshifted outflowing gas coming toward us from a nearly face-on galaxy

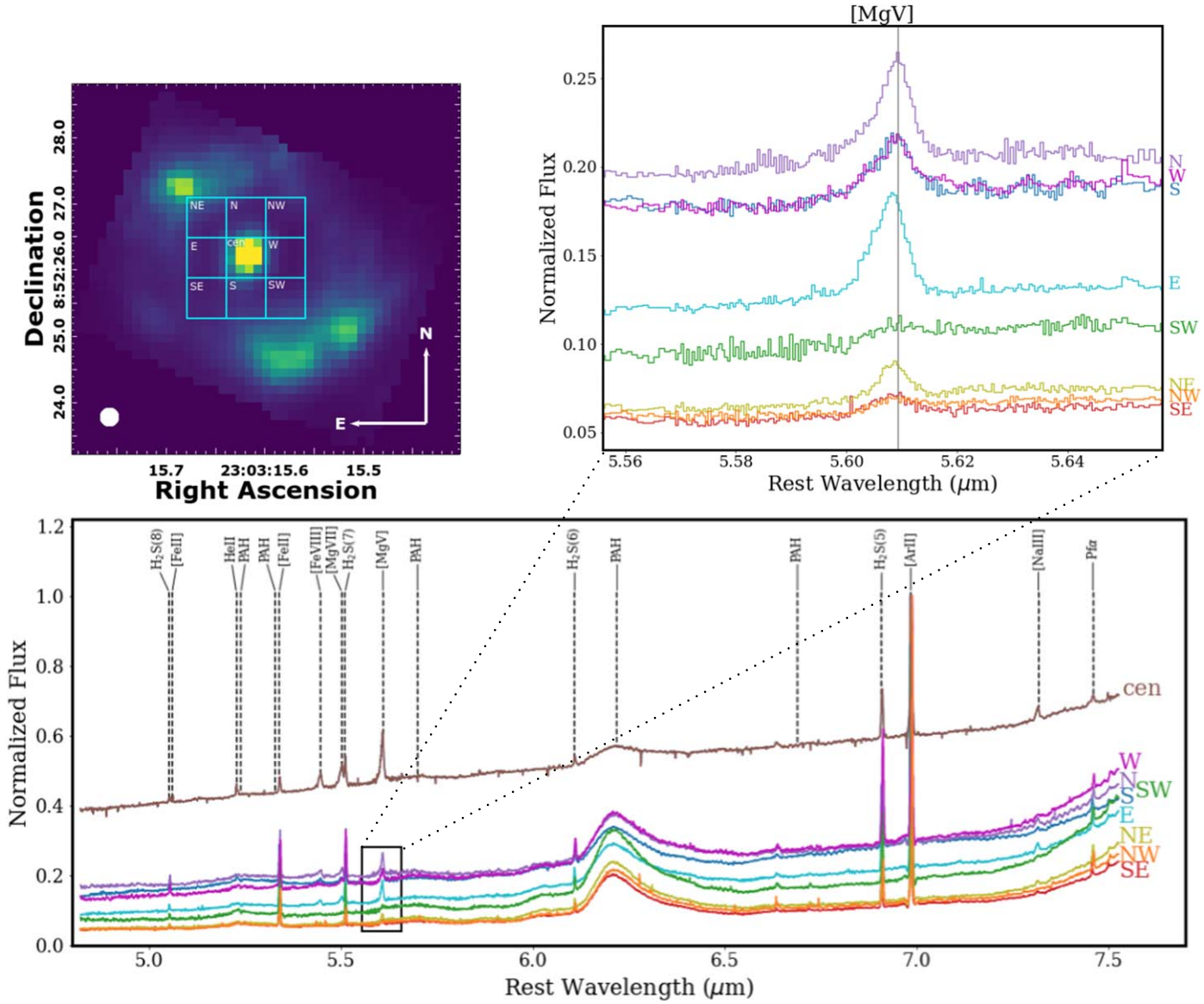

Figure 2. (Top left) Extraction grid (cyan) overlaid on the Channel 1 flux image at 7.1 μm. Each extraction region is 0.″6 on a side, capturing the inner ISM region in this 3 × 3 grid. The PSF FWHM is marked with a filled circle in the bottom-left corner. (Bottom) The Ch 1 short–medium–long stitched spectra extracted from the grid, each labeled by its direction relative to the center "cen." Spectral features are labeled; the spectra are normalized at [Ar II] λ6.99 μm for ease of comparison. A box around coronal line [Mg V] λ5.61 μm is drawn. (Inset) A zoomed-in view of the spectral region centered on [Mg V]. A vertical line at 5.609 μm as defined based on the peak of [Mg V] at the central grid indicates the systemic velocity. [Mg V] is present in most of the inner ISM regions (except for NW and SW); its blueshifted flux is most pronounced in the E.

with an inclination angle of 45° (Davies et al. 2004), which is consistent with our measured i of 51° based on the ring structure. The [Mg V] observations further support the picture in which the circumnuclear obscuration is roughly in the same plane as the galaxy's large-scale disk.

To place our findings in the context of literature results, we consider the scales of the outflows detected with different instruments and tracers. Robleto-Orús et al. (2021) found an outflow as characterized by blueshifted [O III] λ5007 Å extending 531 pc from the nucleus. Resolved at similar scales to our MIRI/MRS data, the [O III] outflow may be more extended than the coronal wind we detect in [Mg V] because it is more easily excited (with IP = 35 eV) and more extincted at the center. On the other hand, the biconically illuminated [Si VI] λ1.96 μm outflow presented by Müller-Sánchez et al. (2011) has an E–W orientation, but at a much smaller scale close to the AGN. The entire [Si VI] emission (IP = 167 eV) falls within the central 1−2 spaxels of MIRI/MRS. The mid-infrared coronal outflow we find could have physical connection with the X-ray warm absorber in this AGN in terms of location and ionization condition (Blustin et al. 2007). Our results suggest a scenario where the high-ionization outflow detected by JWST likely bridges the nuclear-scale (<100 pc) coronal-line region outflow and the larger-scale narrow-line region winds. The outflow appears one-sided because it is approaching us nearly face on; the projected size of a potentially receding red-side cone behind the AGN may be too small to be spatially resolved by MIRI (Figure 3). Even though there may be a hint of a redshifted wing in the W spectrum (Figure 2), the S/N is too weak in the individual spaxels for a robust spectral fit. The redshifted wind may simply be obscured by dense, intervening ISM. Alternatively, the outflow may also appear asymmetric if an inclined jet is pushing on the gas in the

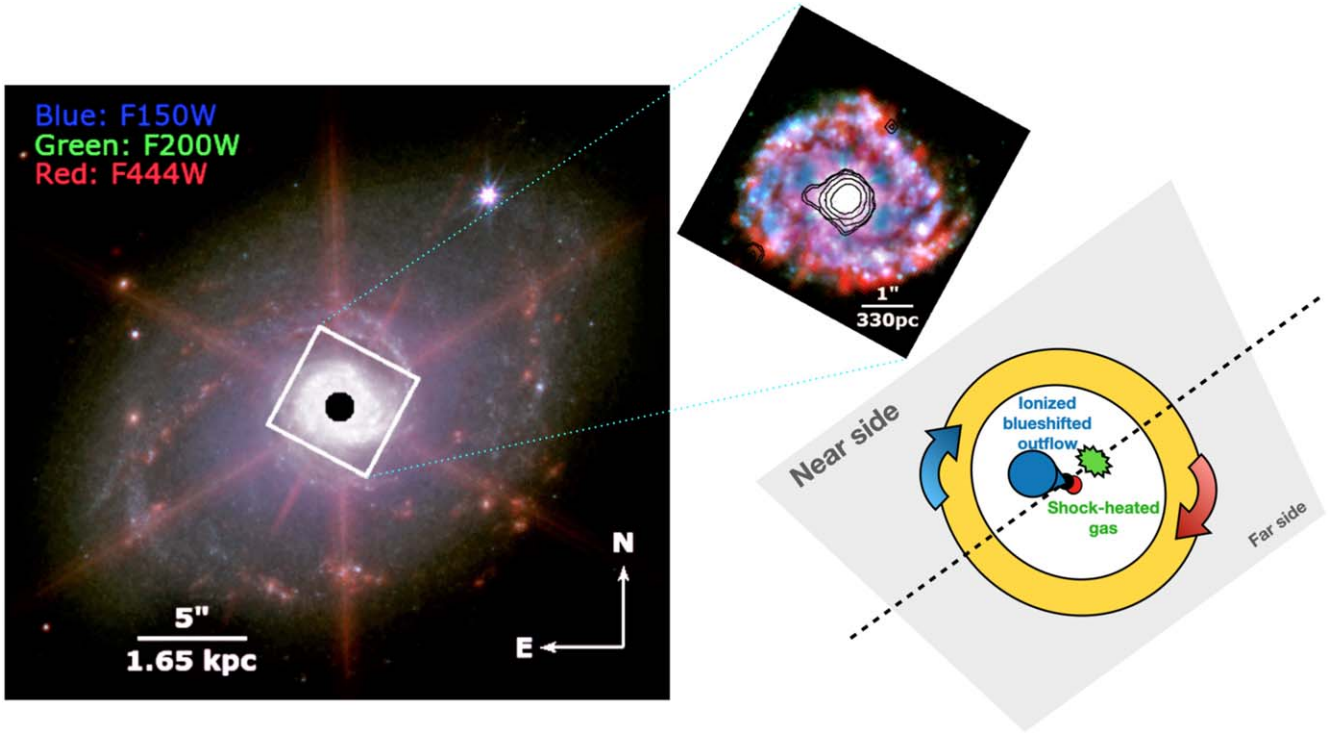

Figure 3. (Left) Three-color F150W/F200W/F444W NIRCam full-array image of NGC 7469 showing the large-scale spiral-arm structures. The inner core is saturated and thus masked out. The overlaid box shows the subarray region. (Inset) Three-color F150W/F200W/F444W NIRCam subarray image showing the star-forming ring around the central nucleus. A 1″ (330 pc) scale bar is shown for comparison. The black contours indicate the intensity of the blueshifted component of the coronal line [Mg V], most of which is coming toward us from the central AGN with a slight eastward extension. (Right) A cartoon schematic showing a nearly face-on outflow that appears one-sided and mostly in blueshift (blue cone). The inclined star-forming ring (near side in the N and far side in the S) is rotating clockwise. Gas is shock-heated on the W side, representing the interaction region where the outflow plows through the ISM of the galaxy. Components are not drawn to scale but merely to illustrate a plausible scenario based on the observed dynamics of the outflow, the inner ISM region, and the ring.

Table 1
Emission-line Flux Densities in MRS Channel 1

Location	H_2 S(5)	H_2 S(6)	H_2 S(7)	PAH 6.2 μm	[Fe II] λ5.34 μm	Pfα
E	1.97 ± 0.05	0.42 ± 0.05	0.90 ± 0.08	83.82 ± 6.49	1.28 ± 0.06	0.25 ± 0.03
N	3.15 ± 0.09	0.67 ± 0.05	1.99 ± 0.12	93.40 ± 3.48	1.73 ± 0.09	0.28 ± 0.03
NE	1.76 ± 0.06	0.29 ± 0.06	0.81 ± 0.07	156.27 ± 4.84	1.95 ± 0.09	0.49 ± 0.03
cen	3.70 ± 0.13	0.82 ± 0.10	1.95 ± 1.09	121.82 ± 32.01	2.00 ± 0.14	$\cdots \pm \cdots$
NW	1.26 ± 0.06	0.24 ± 0.02	0.68 ± 0.06	103.58 ± 5.36	1.49 ± 0.08	0.36 ± 0.03
S	4.88 ± 0.23	1.23 ± 0.19	2.50 ± 0.29	235.51 ± 7.74	4.21 ± 0.26	0.86 ± 0.15
SE	1.52 ± 0.09	0.27 ± 0.07	0.61 ± 0.08	173.99 ± 5.47	2.79 ± 0.13	0.66 ± 0.09
SW	4.46 ± 0.11	0.92 ± 0.14	2.30 ± 0.20	350.55 ± 7.97	5.73 ± 0.27	0.83 ± 0.11
W	7.89 ± 0.18	1.75 ± 0.11	4.56 ± 0.22	178.10 ± 9.80	3.77 ± 0.22	0.53 ± 0.08

Note. All flux densities are in units of 10^{-23} W m^{-2} pc^{-2}. The aperture used for the grid extraction is $0\farcs6 \times 0\farcs6$. Pfα is not well detected at the center and thus its measurement is omitted.

disk (e.g., in NGC 1052; Fernández-Ontiveros et al. 2019). While NGC 7469 may host a radio core–jet structure as resolved by the Very Large Array (Orienti & Prieto 2010), no evidence of a radio jet–ISM interaction has yet been found in its nuclear region (Xu & Wang 2022).

4.2. ISM excitation

Our MIRI/MRS observations allow us, for the first time, to examine the high-ionization outflow identified here in [Mg V] at $r < 300$ pc in detail. We search for evidence that indicates how the outflow may impact its surroundings. The mid-infrared rotational transitions of H_2, when coupled with measurements of the PAH emission, provide a robust diagnostic of the excitation conditions and help determine the mechanism responsible for exciting the H_2 lines (Higdon et al. 2006; Ogle et al. 2010; Guillard et al. 2012; Cluver et al. 2013). Young massive stars may heat both PAHs and H_2 in photodissociation regions (PDRs), but shocks arising from outflows or X-ray emission from AGNs effectively dissociate PAH molecules and small grains (Jones et al. 1996). Empirically, low-luminosity star-forming galaxies exhibit a limited range of luminosity ratio $L(H_2)/L(PAH)$ over several orders of magnitude in $L(H_2)$ while those for AGNs display line ratios $\sim$15 times greater (Roussel et al. 2007). Thus, the line ratio $L(H_2)/L(PAH)$ has been used to distinguish between AGNs, stars, and shocks as the driver of molecular emission in

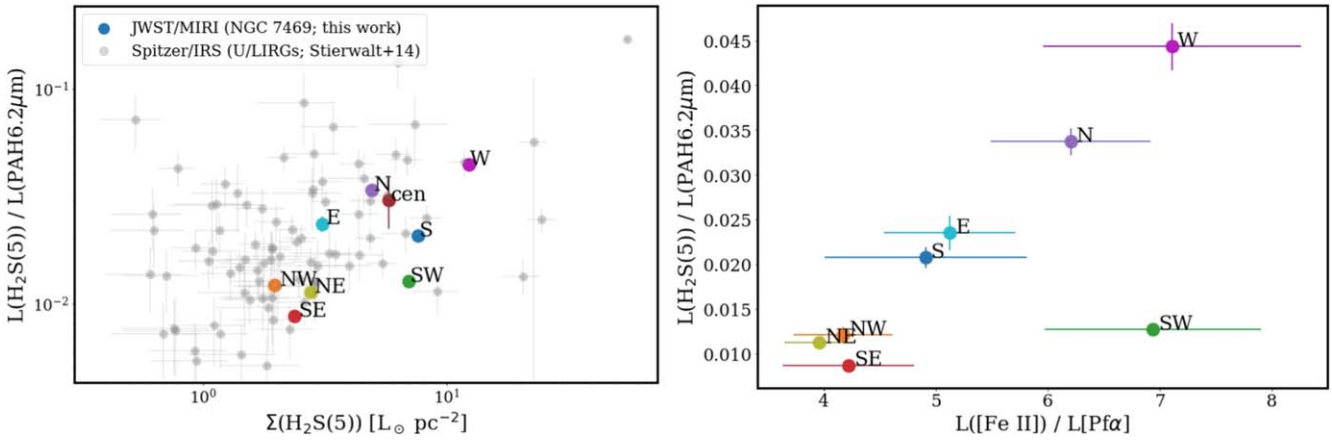

Figure 4. (Left) $L(H_2)/L(PAH)$ vs. H_2 luminosity density diagnostics diagram showing the data points corresponding to different parts of the inner ISM region. The gray points are local LIRGs from Stierwalt et al. (2014) for which these line transitions are detected and H_2 luminosities normalized by the extraction aperture; upper limits have been excluded. The inner ISM in NGC 7469 tends to be bright in H_2 but spans a range of $L(H_2)/L(PAH)$ values nearly representative of the local LIRGs. (Right) The same $L(H_2)/L(PAH)$ line ratios plotted against $L([Fe\ II])/L(Pf\alpha)$. The correlation seen here ($\rho = 0.62^{+0.26}_{-0.40}$ with a p-value of 0.10 for all the points; $\rho = 0.86^{+0.09}_{-0.19}$, with a p-value of 0.01 excluding the SW outlier) suggests that shocks traced by [Fe II] are correlated with the shocked H_2 gas. Pfα is not well detected in the central spectrum and thus the center point is excluded from this plot.

extreme environments such as LIRGs (Stierwalt et al. 2014; U et al. 2019).

Ideally, the total power in the warm H_2 and all forms of PAH lines should be used in any analysis of PDR heating, given that the bulk of the molecular gas mass may be traced by the lower rotational H_2 transitions. However, to take advantage of the high spatial resolution in MIRI Ch 1 and minimize contamination in the inner ISM region from the nucleus and the ring, we opt to confine our analysis of $L(H_2)/L(PAH)$ to the lines present in this channel, recognizing the potential limitations. In Ch 1 MRS data cube (Figure 2), four H_2 transitions are identified: S(5) λ6.91 μm is detected and appears prominent in all the extracted spectra; S(6) λ6.11 μm, while detected, sits on top of a prominent PAH feature at 6.2 μm and may be dominated by PAHs at certain locations; S(7) λ5.51 μm may be partially blended with [Mg VII] λ5.5 μm; and S(8) λ5.05 μm is comparatively weak. For these reasons, the S(5) line is the most optimal line among the possibilities. Its proximity to PAH 6.2 μm reduces the risk of potential calibration differences between subbands and differential extinction, so we focus on using this pair of features for the $L(H_2)/L(PAH)$ diagnostic. We note that close to the AGN (<300 pc), the H_2 gas is expected to be quite hot (~900–1100K; Lambrides et al. 2019; Pereira-Santaella et al. 2022) and is dominated by AGN heating in the central ~100 pc (Armus et al. 2022), so the S(5) line likely carries much of the H_2 luminosity, justifying our reliance on this line to measure the $L(H_2)/L(PAH)$ ratio.

Figure 4 (left) shows the $L(H_2)/L(PAH)$ distribution versus H_2 luminosity density for the different locations within the inner ISM. The first result is that the corner points (NW, NE, SE, and SW) all have lower $L(H_2)/L(PAH)$ ratios than the other locations. Examining the spectra in Figure 2, the PAH features are more prominent at the corner locations that contain a larger fractional emission from the ring than at the E–W or N–S locations. This is expected, since PAH emission mostly originates from PDRs and, for some galaxy populations and/or environments, can be used as star formation rate tracers (e.g., Peeters et al. 2004). In contrast, the H_2 emission is relatively weaker in the ring, as seen in Figure 1, in agreement with what is expected from actively star-forming regions.

For comparison, we have plotted in Figure 4 the integrated Spitzer/IRS data points for a sample of local LIRGs (Stierwalt et al. 2014) from the Great Observatories All-sky LIRGs Survey (GOALS; Armus et al. 2009). Because the angular-size aperture ($3\farcs7 \times 9\farcs5$) used to extract the Spitzer/IRS spectra is much larger than that of our extraction grid size, we show the H_2 luminosity surface density, Σ_{H2}, in the x-axis instead of luminosity for a more direct comparison with the Spitzer/IRS values. Our data points span a broad range in $L(H_2)/L(PAH)$ of the GOALS LIRGs and are consistent with the more H_2-bright sources for a given $L(H_2)/L(PAH)$ value. This shift may be due to the fact that the global values from Spitzer/IRS are uniformly weighted and encompass many star-forming regions and obscured AGN sources, while our resolved data points represent the inner ISM region close to the Seyfert nucleus in NGC 7469 where H_2 is prominently detected.

The inner ISM region does not host bright star-forming regions and therefore PDR models are not applicable, but X-rays from the AGN and shocks from the outflow can heat the molecular gas (Petric et al. 2018; Minsley et al. 2020). Since iron is highly depleted onto grains, [Fe II] is a commonly adopted tracer of shock-excited gas where grains have been processed by outflows or other ionizing sources (see references in reviews by Sajina et al. (2022) and U (2022). Infrared studies of supernova remnants indicate that not only do they produce H_2 lines as luminous as bright star-forming regions, they are also associated with enhanced [Fe II]/Brγ relative to typical H II regions (Oliva et al. 1989). The latter observation has been predicted by theoretical models of shock fronts (McKee et al. 1984), where the ratio of [Fe II] to hydrogen is deemed a useful indicator of the efficiency of the shock front in destroying dust grains (Hollenbach & McKee 1989). Here, we examine the ratio of $L([Fe\ II])/L(Pf\alpha)$ given that the H recombination line Pfund α traces star formation, provides a calibration baseline, and is detected in Ch 1.

Figure 4 (right) shows $L(H_2)/L(PAH)$ plotted as a function of $L([Fe\ II])/L(Pf\alpha)$, which appears to be well correlated with the exception of the SW region. We compute a correlation for all the data points using `pymccorrelation` (Privon et al. 2020) with 10^4 bootstrapping iterations to estimate the uncertainties. We determine the Pearson's correlation coefficient $\rho = 0.62^{+0.26}_{-0.40}$,

with a p-value of 0.10 driven mostly by the outlier point at SW and the large uncertainties of Pfα. If we exclude SW (which shows the peakiest PAH 6.2 μm profile and the most extreme slope on the red end of the Ch1 spectra where Pfα is located; see Figure 2), the resulting coefficient becomes $\rho = 0.86^{+0.09}_{-0.19}$, with a p-value of 0.01, suggesting that [Fe II] and H_2 at the W and N locations are likely excited by the same shocks driven by the outflow. This correlation between [Fe II] and H_2 in (U)LIRGs has been studied by Hill & Zakamska (2014), who also inferred that shocks, including AGN-driven ones, are the likely source of H_2 heating.

The most extreme region, W, which partially overlaps the region of high H_2 and [Fe II] velocity dispersion (Figure 1), is, interestingly, on the opposite side of the center from the blueshifted coronal gas. It is possible that the H_2 and [Fe II] are regions of high velocity dispersion that represent regions where the receding, partially obscured part of the outflow is plowing into the dense ISM and releasing [Fe II] into the gas phase. A strong correlation between [Fe II] and H_2 may be associated with sites of supernova remnants, where [Fe II] is produced in radiative shocks after grain destruction as the supernova remnant propagates (Hill & Zakamska 2014). Given the extremely high-velocity coronal-line components detected in the nuclear spectrum (Armus et al. 2022), the AGN itself is likely driving the highly ionized wind detected here in [Mg V], which deposits energy into the ISM via shocks in the W and NW regions where the dispersion of the warm molecular gas and the $L(H_2)/L(\mathrm{PAH})$ ratios are highest. It is somewhat surprising, given the location of the high-dispersion H_2 gas, that the NW spectrum is low in Figure 4 (left). However, this extraction region is large and partially intersects the inner edge of the ring, where the H_2 is weak and the PAH is bright. Examining the individual pixels in this region indicates the $L(H_2)/L(\mathrm{PAH})$ ratio changes by a factor of 8 as one moves from the upper right to the lower left of this region. Therefore, the area of maximum dispersion in the NW would indeed be located much higher in Figure 4, close to the position of region W, consistent with our simple model. A more detailed analysis of these regions will be performed in a subsequent paper using a spectral decomposition tool designed to produce accurate line-ratio maps on finer scales.

5. Summary

In this Letter, we present new JWST MIRI MRS observations of NGC 7469 and focus on the analysis of the inner ISM region between the central AGN and the starburst ring. The high spatial and spectral resolution available with the new IFS capability of MIRI enables a detailed investigation of the rotational H_2, low-, and high-ionization fine-structure lines, and dust features at mid-infrared wavelengths for the first time. We summarize our findings below.

1. The morphology of the low-ionization [Fe II] and [Ar II] lines is bright in the nucleus and in the starburst ring, showing several star-forming clumps and regions of enhanced emission. The H_2, in contrast, is strongly peaked on the nucleus and surrounding ISM, and is relatively weak in the starburst ring.
2. The [Mg V] emission line is resolved and shows a broad, blueshifted component that is likely associated with the coronal-line outflow in NGC 7469. The blueshifted highly ionized outflow traced by [Mg V], has a nearly face-on geometry that is strongly peaked on the nucleus, with an extension that reaches about 400 pc to the east. The [Mg V] gas has a median line-of-sight velocity $v_{\mathrm{med}} = -205$ km s^{-1} and reaches as high as -650 km s^{-1} close to the AGN.
3. There are regions of enhanced velocity dispersion in H_2 and [Fe II] ~ 180 pc from the AGN that also feature excited $L([\mathrm{Fe\ II}])/L(\mathrm{Pf}\alpha)$ and $L(H_2)/L(\mathrm{PAH})$ ratios, most clearly seen to the N and W. We identify these regions as the locations where the outflow is depositing energy into the dense interstellar gas via shocks, between the nucleus and the starburst ring.

Such a detailed view of the mid-infrared gas dynamics within the central region of a dusty LIRG nucleus is made possible for the first time, fully demonstrating the high spatial and spectral resolution plus the high-sensitivity integral-field capability of JWST.

We thank Jim Braatz, Patrick Ogle, Andreea Petric, and the anonymous reviewer for suggestions that significantly improved the paper. This work is based on observations made with the NASA/ESA/CSA JWST. The research was supported by NASA grant JWST-ERS-01328. The data were obtained from the Mikulski Archive for Space Telescopes at the Space Telescope Science Institute, which is operated by the Association of Universities for Research in Astronomy, Inc., under NASA contract NAS 5-03127 for JWST. These observations are associated with program #1328 and can be accessed via 10.17909/0fe2-cf33. V.U acknowledges funding support from NASA Astrophysics Data Analysis Program (ADAP) grant 80NSSC20K0450. The Flatiron Institute is supported by the Simons Foundation. H.I. and T.B. acknowledge support from JSPS KAKENHI grant No. JP21H01129 and the Ito Foundation for Promotion of Science. A.M.M. acknowledges support from the National Science Foundation under grant No. 2009416. A.S.E. and S.L. acknowledge support from NASA grant HST-GO15472. Y.S. was funded in part by the NSF through the Grote Reber Fellowship Program administered by Associated Universities, Inc./National Radio Astronomy Observatory. The National Radio Astronomy Observatory is a facility of the National Science Foundation operated under cooperative agreement by Associated Universities, Inc. S.A. gratefully acknowledges support from an ERC Advanced grant 789410, from the Swedish Research Council and from the Knut and Alice Wallenberg (KAW) Foundation. K.I. acknowledges support by the Spanish MCIN under grant PID2019-105510GB-C33/AEI/10.13039/501100011033. F.M-S. acknowledges support from NASA through ADAP award 80NSSC19K1096. Finally, this research has made use of the NASA/IPAC Extragalactic Database (NED), which is operated by the Jet Propulsion Laboratory, California Institute of Technology, under contract with the National Aeronautics and Space Administration.

Facility: JWST (NIRCam and MIRI).

Software: astropy (Astropy Collaboration et al. 2013, 2018), Cosmology calculator (Wright 2006), JWST Science Calibration Pipeline (Bushouse et al. 2022), ifscube (Ruschel-Dutra & Dall'Agnol De Oliveira 2020; Ruschel-Dutra et al. 2021), BADASS (Sexton et al. 2021), CAFE (Marshall et al. 2007, Díaz-Santos et al. 2022, in preparation), JDAVis (Lim et al. 2022), PAfit (Krajnovic et al. 2006), pymccorelation (Curran 2014; Privon et al. 2020).

Appendix
Fitting the Coronal Line

As mentioned in Section 2, we conduct an in-depth investigation of the coronal line [Mg V] over the entire Ch1 FOV using the BADASS (Sexton et al. 2021) software package. We fit one- and two-component Gaussian profiles to the line spaxel by spaxel (e.g., Figure A1) and generate their resulting flux, velocity, and velocity dispersion maps (Figure A2). The velocity dispersion maps have been corrected for instrumental broadening ($\sigma_{\rm inst} = 36.5$ km s^{-1}). The flux map of the secondary broad component of [Mg V] (bottom-left panel of Figure A2) is overplotted on NIRCam images as contours in Figure 3 to indicate the high-ionization outflow.

We note that this two-component spectral fitting was only applied to [Mg V] on a per-spaxel basis in this work to generate the moment maps. In a companion paper (Armus et al. 2022), multicomponent fitting is applied to all the emission lines in the full MIRI/MRS nuclear spectrum extracted from a small aperture on the AGN.

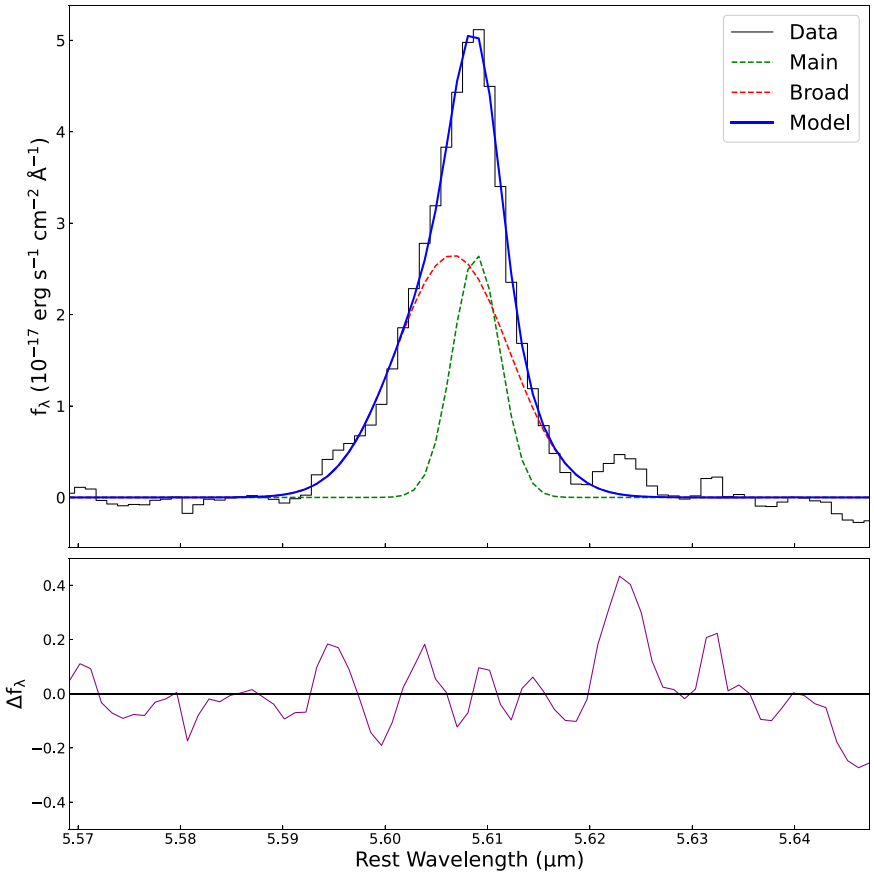

Figure A1. (Top) Example two-component Gaussian fit to the [Mg V] from one spaxel at the center. Two Gaussian components—a main (green dashed) and a broad (red dashed) one—are needed to fit the "outflow" region of the map. The residual resulting from subtracting Model (blue) from Data (black) is shown in the bottom plot.

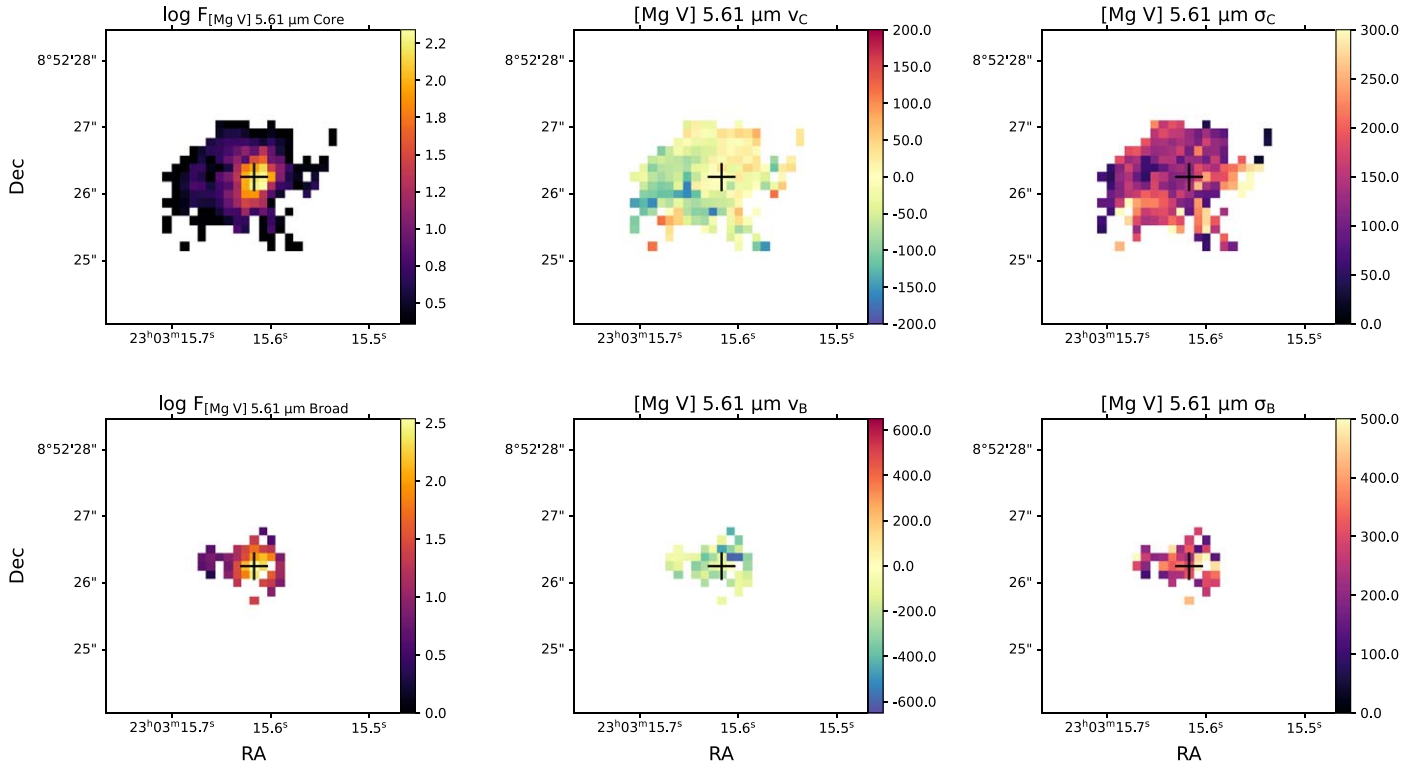

Figure A2. Flux (left, in log 10^{-17} erg cm^{-2} s^{-1} px^{-1}), velocity (middle, in km s^{-1}), and velocity dispersion (right, in km s^{-1}) maps of the core, narrow Gaussian component (top) and of the second, broad, blueshifted component (bottom) of [Mg V]. The cross marks the location of the central AGN defined at the continuum. The velocity dispersion maps have been corrected for instrumental broadening. Note that the color bar on these maps are all different in order to optimize visualizing the range of values spanned by each of the maps. North is up and east is to the left.

ORCID iDs

Vivian U https://orcid.org/0000-0002-1912-0024
Thomas Lai https://orcid.org/0000-0001-8490-6632
Marina Bianchin https://orcid.org/0000-0002-6570-9446
Raymond P. Remigio https://orcid.org/0000-0002-0164-8795
Lee Armus https://orcid.org/0000-0003-3498-2973
Kirsten L. Larson https://orcid.org/0000-0003-3917-6460
Tanio Díaz-Santos https://orcid.org/0000-0003-0699-6083
Aaron Evans https://orcid.org/0000-0003-2638-1334
Sabrina Stierwalt https://orcid.org/0000-0002-2596-8531
David R. Law https://orcid.org/0000-0002-9402-186X
Matthew A. Malkan https://orcid.org/0000-0001-6919-1237
Sean Linden https://orcid.org/0000-0002-1000-6081
Yiqing Song https://orcid.org/0000-0002-3139-3041
Paul P. van der Werf https://orcid.org/0000-0001-5434-5942
Tianmu Gao https://orcid.org/0000-0002-1158-6372
George C. Privon https://orcid.org/0000-0003-3474-1125
Anne M. Medling https://orcid.org/0000-0001-7421-2944
Loreto Barcos-Muñoz https://orcid.org/0000-0003-0057-8892
Christopher C. Hayward https://orcid.org/0000-0003-4073-3236
Hanae Inami https://orcid.org/0000-0003-4268-0393
Jeff Rich https://orcid.org/0000-0002-5807-5078
Susanne Aalto https://orcid.org/0000-0002-5828-7660
Philip Appleton https://orcid.org/0000-0002-7607-8766
Thomas Bohn https://orcid.org/0000-0002-4375-254X
Torsten Böker https://orcid.org/0000-0002-5666-7782
Michael J. I. Brown https://orcid.org/0000-0002-1207-9137
Vassilis Charmandaris https://orcid.org/0000-0002-2688-1956
Luke Finnerty https://orcid.org/0000-0002-1392-0768
Justin Howell https://orcid.org/0000-0001-6028-8059
Kazushi Iwasawa https://orcid.org/0000-0002-4923-3281
Francisca Kemper https://orcid.org/0000-0003-2743-8240
Jason Marshall https://orcid.org/0000-0001-7712-8465
Joseph M. Mazzarella https://orcid.org/0000-0002-8204-8619
Jed McKinney https://orcid.org/0000-0002-6149-8178
Francisco Muller-Sanchez https://orcid.org/0000-0002-2713-0628
Eric J. Murphy https://orcid.org/0000-0001-7089-7325
David Sanders https://orcid.org/0000-0002-1233-9998
Jason Surace https://orcid.org/0000-0001-7291-0087

References

Armus, L., Charmandaris, V., & Soifer, B. T. 2020, NatAs, 4, 467
Armus, L., Lai, T., U, V., et al. 2022, arXiv:2209.13125
Armus, L., Mazzarella, J. M., Evans, A. S., et al. 2009, PASP, 121, 559
Astropy Collaboration, Price-Whelan, A. M., Sipőcz, B. M., et al. 2018, AJ, 156, 123
Astropy Collaboration, Robitaille, T. P., Tollerud, E. J., et al. 2013, A&A, 558, A33
Blustin, A. J., Kriss, G. A., Holczer, T., et al. 2007, A&A, 466, 107
Bohn, T., Inami, H., Diaz-Santos, T., et al. 2022, arXiv:2209.04466
Bushouse, H., Eisenhamer, J., Dencheva, N., et al. 2022, spacetelescope/jwst: JWST 1.6.2, 1.6.2, Zenodo, doi:10.5281/zenodo.6984366
Cazzoli, S., Gil de Paz, A., Márquez, I., et al. 2020, MNRAS, 493, 3656
Cluver, M. E., Appleton, P. N., Ogle, P., et al. 2013, ApJ, 765, 93
Curran, P. A. 2014, arXiv:1411.3816
Davies, R. I., Tacconi, L. J., & Genzel, R. 2004, ApJ, 602, 148

De Breuck, C., Williams, R. J., Swinbank, M., et al. 2014, A&A, 565, A59
Díaz-Santos, T., Alonso-Herrero, A., Colina, L., Ryder, S. D., & Knapen, J. H. 2007, ApJ, 661, 149
Falstad, N., Aalto, S., König, S., et al. 2021, A&A, 649, A105
Ferguson, J. W., Korista, K. T., & Ferland, G. J. 1997, ApJS, 110, 287
Fernández-Ontiveros, J. A., López-Gonzaga, N., Prieto, M. A., et al. 2019, MNRAS, 485, 5377
Genzel, R., Weitzel, L., Tacconi-Garman, L. E., et al. 1995, ApJ, 444, 129
Guillard, P., Ogle, P. M., Emonts, B. H. C., et al. 2012, ApJ, 747, 95
Higdon, S. J. U., Armus, L., Higdon, J. L., Soifer, B. T., & Spoon, H. W. W. 2006, ApJ, 648, 323
Hill, M. J., & Zakamska, N. L. 2014, MNRAS, 439, 2701
Hollenbach, D., & McKee, C. F. 1989, ApJ, 342, 306
Inami, H., Armus, L., Charmandaris, V., et al. 2013, ApJ, 777, 156
Izumi, T., Nguyen, D. D., Imanishi, M., et al. 2020, ApJ, 898, 75
Jones, A. P., Tielens, A. G. G. M., & Hollenbach, D. J. 1996, ApJ, 469, 740
Krajnovic, D., Cappellari, M., De Zeeuw, P. T., & Copin, Y. 2006, MNRAS, 366, 787
Labiano, A., Argyriou, I., Álvarez-Márquez, J., et al. 2021, A&A, 656, A57
Lai, T. S. Y., Armus, L., U, V., et al. 2022, arXiv:2209.06741
Lambrides, E. L., Petric, A. O., Tchernyshyov, K., Zakamska, N. L., & Watts, D. J. 2019, MNRAS, 487, 1823
Landt, H., Bentz, M. C., Ward, M. J., et al. 2008, ApJS, 174, 282
Lim, P. L., O'Steen, R., Earl, N., et al. 2022, spacetelescope/jdaviz: v2.8.0, v2.8.0, Zenodo, doi:10.5281/zenodo.6877878
Marshall, J. A., Herter, T. L., Armus, L., et al. 2007, ApJ, 670, 129
Mattila, S., Väisänen, P., Farrah, D., et al. 2007, ApJL, 659, L9
McKee, C. F., Chernoff, D. F., Hollenbach, D. J., et al. 1984, in Astrophysics and Space Science Library, Galactic and Extragalactic Infrared Spectroscopy, Vol. 108 ed. M. F. Kessler & J. P. Phillips, 103
Minsley, R., Petric, A., Lambrides, E., et al. 2020, ApJ, 894, 157
Müller-Sánchez, F., Prieto, M. A., Hicks, E. K. S., et al. 2011, ApJ, 739, 69
Nguyen, D. D., Izumi, T., Thater, S., et al. 2021, MNRAS, 504, 4123
Ogle, P., Boulanger, F., Guillard, P., et al. 2010, ApJ, 724, 1193
Oliva, E., Moorwood, A. F. M., & Danziger, I. J. 1989, A&A, 214, 307
Orienti, M., & Prieto, M. A. 2010, MNRAS, 401, 2599
Oschmann, J. M., Clampin, M., Fazio, G. G., et al. 2014, Proc. SPIE, 9143, 91433X
Peeters, E., Spoon, H. W. W., & Tielens, A. G. G. M. 2004, ApJ, 613, 986
Pereira-Santaella, M., Álvarez-Márquez, J., García-Bernete, I., et al. 2022, A&A, 665, L11
Pérez-Torres, M., Mattila, S., Alonso-Herrero, A., Aalto, S., & Efstathiou, A. 2021, A&ARv, 29, 2
Petric, A. O., Armus, L., Flagey, N., et al. 2018, AJ, 156, 295
Pontoppidan, K., Blome, C., Braun, H., et al. 2022, ApJ, 936, 14
Privon, G. C., Ricci, C., Aalto, S., et al. 2020, ApJ, 893, 149
Rieke, G. H., Wright, G. S., Böker, T., et al. 2015, PASP, 127, 584
Riffel, R. A., Dors, O. L., Armah, M., et al. 2021, MNRAS, 501, L54
Robleto-Orús, A. C., Torres-Papaqui, J. P., Longinotti, A. L., et al. 2021, ApJL, 906, L6
Roussel, H., Helou, G., Hollenbach, D. J., et al. 2007, ApJ, 669, 959
Ruschel-Dutra, D., & Dall'Agnol De Oliveira, B. 2020, danielrd6/ifscube: Modeling, v1.1, Zenodo, Zenodo, doi:10.5281/zenodo.4065550
Ruschel-Dutra, D., Storchi-Bergmann, T., Schnorr-Muller, A., et al. 2021, MNRAS, 507, 74
Sajina, A., Lacy, M., & Pope, A. 2022, Univ, 8, 356
Sexton, R. O., Matzko, W., Darden, N., Canalizo, G., & Gorjian, V. 2021, MNRAS, 500, 2871
Song, Y., Linden, S. T., Evans, A. S., et al. 2021, ApJ, 916, 73
Stierwalt, S., Armus, L., Charmandaris, V., et al. 2014, ApJ, 790, 124
Stierwalt, S., Armus, L., Surace, J. A., et al. 2013, ApJS, 206, 1
Swinbank, A. M., Smail, I., Sobral, D., et al. 2012, ApJ, 760, 130
U, V. 2022, Univ, 8, 392
U, V., Medling, A., Sanders, D., et al. 2013, ApJ, 775, 115
U, V., Medling, A. M., Inami, H., et al. 2019, ApJ, 871, 166
Väisänen, P., Reunanen, J., Kotilainen, J., et al. 2017, MNRAS, 471, 2059
Veilleux, S., Maiolino, R., Bolatto, A. D., & Aalto, S. 2020, A&ARv, 28, 2
Wright, E. L. 2006, PASP, 118, 1711
Xu, X., & Wang, J. 2022, ApJ, 933, 110